Journal of Applied Fluid Mechanics, Vol. 18, No. 1, pp. 274-289, 2025.
Available online at www.jafmonline.net, ISSN 1735-3572, EISSN 1735-3645.
https://doi.org/10.47176/jafm.18.1.2590

Effects of Inlet Tip Clearance on Internal Flow Characteristic and Aerodynamic Performance of Centrifugal Compressor

Y. Zhang[1], J. Chen[1], Y. Shu[2], Z. Wang[1], H. Yang[1] and Y. Wei[1,2†]

[1] Zhejiang Key Laboratory of Multiflow and Fluid Machinery, Zhejiang Sci-Tech University, Hangzhou, Zhejiang 310018, China
[2]State Key Laboratory of High-end Compressor and System Technology, General Machinery and Key Basic Component Innovation Center (Anhui) Co., Ltd, Hefei General Machinery Research Institute Co., Ltd., Hefei, Anhui 230031, China

†Corresponding Author Email: yikunwei@zstu.edu.cn

ABSTRACT

In this study, numerical simulations of centrifugal compressors are carried out using ANSYS-CFX software. The focus lies in investigating the impact of the inlet tip-clearance (ITC) on the characteristics of the internal complex flow and the aerodynamic performance of centrifugal compressors. Specifically, the paper mainly emphasizes the influence of ITC on the polytropic efficiency and total pressure ratio of a centrifugal compressor, as well as the variations in velocity and pressure at the blade tip, the spatiotemporal evolution of the tip-leakage vortex (TLV), and fluctuations in pressure and velocity downstream of the passage near the blade surface. Analysis of tip-leakage flow (TLF) and TLV motion patterns at rated operating conditions reveals the spatiotemporal evolution within one revolution. Results from Fast Fourier Transform (FFT) spectrum analysis indicate that the TLV motion pattern may be affected by the ITC size. The fluid flow resistance and backflow in the blade tip region are gradually reduced, the flow field stability is effectively enhanced, and the reflux vortex at the volute outlet is eliminated, thereby the working range of the centrifugal compressor is effectively extended by decreasing the ITC. The aerodynamic performance of the centrifugal compressor is effectively increased in the range of the medium and high flow rates by decreasing ITC. Additionally, it is observed that pressure, velocity, and load in the blade tip region do not exhibit a linear relationship with ITC, resulting in a nonlinear change in aerodynamic performance concerning ITC. Pressure and velocity spectrum analysis suggests that the effect of TLF is stronger at the top of the flow passage compared to the middle. Moreover, with the increase of ITC, the effect of TLF decreases at the middle and top of the pressure side (PS) while increasing at the bottom of PS and the suction side (SS).

Article History

Received January 25, 2024
Revised July 24, 2024
Accepted August 3, 2024
Available online November 6, 2024

Keywords:

Numerical simulation
Centrifugal compressor
Inlet Tip Clearance (ITC)
Spatiotemporal evolution
Fast Fourier Transform (FFT)
Nonlinear relationship

1. INTRODUCTION

Centrifugal compressors find widespread applications in turbine engines, automobile turbochargers, micro-gas turbines, and various industrial processes to elevate gas pressure (Jaatinen et al., 2016). The two most common impeller types used in centrifugal compressors are closed and semi-open impellers. Due to their high strength and maximum circumferential velocity, the semi-open impellers are widely preferred in centrifugal compressors (Liu & Chen 2012).

A gap, known as the inlet tip clearance (ITC), is incorporated at the tip of the semi-open centrifugal impeller, the main purpose is to prevent friction and collision between the centrifugal impeller and the housing wall. Nonetheless, the flow from this clearance, when entering the narrow blade passage with the high-speed rotating impeller, triggers additional separation flows, secondary flows, and clearance vortices. This clearance flow significantly influences the aerodynamic performance of the centrifugal compressor (Berdanier & Key 2015; Zhang et al., 2019). Hence, the impact of the ITC on flow characteristics remains a prominent area of research due to the challenges associated with centrifugal compressors (Galindo et al., 2015; Tsoutsanis et al., 2015). Song et al. (2020) studied the effect of axial compressor ITC characteristics on internal flow related to performance. Research suggests that optimal clearances are identified within steady operating ranges.

Nomenclature

Abbreviations

ITC	Inlet Tip Clearance
TLV	Tip-Leakage Vortex
TLF	Tip-Leakage Flow
FFT	Fast Fourier Transform
SST	Shear Stress Transport
PS	Pressure Side
SS	Suction Side
LE	Leading Edge
TE	Trailing Edge
TKE	Turbulent Kinetic Energy

Greek

ρ	density
ε	turbulent dissipation rate
ω	specific dissipation rate

Subscripts

i	tensor symbols
j	tensor symbols
k	turbulence kinetic energy

Symbols

u_i	velocity component
u	macroscopic velocity of the mainstream
t	time
t_0	time for ten revolutions of the impeller
T_1	time for one revolution
G	generation items
R	radius of the impeller, mm
β_{B1}	blade installation angle of the inlet
β_{B2}	blade installation angle of the outlet
v	specific dissipation rate
Y_k	divergent terms
D_ω	orthogonal divergence term
D_1	diameter of impeller inlet
D_2	diameter of impeller outlet
b_2	width of impeller outlet
f_n	blade rotation frequency

Liu et al. (2021) investigated the influence of the ITC law on the pressure ratio and efficiency of centrifugal compressors by numerical simulation and experiment analysis.

The findings show that there is an approximately linear relationship between an increase in ITC and a decrease in the performance of the compressor. Ostad & Kamali (2019) examined the influence of the ITC on the efficiency of axial compressors. The results suggested that altering the clearance height or blade tip shape did not significantly improve compressor performance. Xu et al. (2022) numerically studied the pressure and velocity fluctuation characteristics at the near wall in the ITC flow of an axial compressor. The movement pattern of leakage vortexes may be associated with the blade passage, predominantly affecting the region from the middle to the TE of the flow passage, with minimal impact near the leading edge. Sohail et al. (2020) studied a detailed investigation into the flow field region of inlet tip clearances and their significant impacts on the aerodynamic performance, stable working range, and stability margin of axial compressors by numerical calculation. The findings reveal that increasing the tip clearance adversely affects the polytropic efficiency and total pressure ratio, with the choking point of the rotor decreasing as the ITC increases. Wang et al. (2020) performed a numerical simulation of the design rotation speed by adjusting the trailing edge tip clearance of the centrifugal impeller. The results suggest that, compared to low flow rates, the changes in the trailing edge tip clearance had a noticeable effect on the aerodynamic performance of the centrifugal compressor at high flow rates.

Previous studies have examined the gap effect on internal complex flow and aerodynamic performance of centrifugal compressors in light of tip clearance discussions. However, these studies have not accurately quantified the impact of ITC on compressor internal flow and aerodynamic performance. The quantitative correlation between compressor inlet tip clearance and internal flow remains under exploration to elucidate its influence on compressor internal flow and aerodynamic performance. This paper mainly discusses the influences of ITC on the total pressure ratio and efficiency of centrifugal compressors and provides insights into the physical mechanisms of internal complex flow characteristics. Innovative spatiotemporal correlations of pressure and velocity fluctuations are employed to investigate the transient characteristics of TLF under rated operating conditions. The findings suggest that increasing the inlet tip clearance size may offer valuable insights into expanding the working range of the centrifugal compressor and reducing the load on the top of the blade.

2. NUMERICAL METHODOLOGY

2.1 Governing Equations

The compressible Navier-Stokes (N-S) equations are applied to the motion of the fluid in a centrifugal compressor. The equation of continuity for a compressible fluid is shown as follows:

$$\frac{\partial\rho}{\partial t}+\frac{\partial(\rho u)}{\partial x}+\frac{\partial(\rho v)}{\partial y}+\frac{\partial(\rho w)}{\partial z}=0 \tag{1}$$

The equation of momentum is given as follows:

$$\frac{\partial}{\partial t}(\rho u_i)+\frac{\partial}{\partial x_i}(\rho u_i u_j)=-\frac{\partial_p}{x_i}+\frac{\partial}{x_i}\left(\mu\frac{\partial u_i}{\partial x_i}-\rho\overline{u_i^{'}u_j^{'}}\right)+S_i \tag{2}$$

where ρ is the density of the fluid, u represents the velocity of the mainstream.

The equation of total energy used in the numerical calculation is:

$$\frac{\partial(\rho h_{tot})}{\partial t}-\frac{\partial p}{\partial t}+\nabla\cdot(\rho U h_{tot})=\nabla\cdot(\lambda\nabla T)+\nabla\cdot(U\cdot\tau)+U\cdot S_M+S_E \tag{3}$$

where tot represents the total enthalpy.

$$h_{tot} = h + \frac{1}{2}U^{2} \tag{4}$$

2.2 Turbulence Model

The shear stress transport (SST) turbulence model is a widely used turbulence model in numerical calculations. It keeps the benefits of both the k-epsilon (k-ε) model and the k-omega (k-ω) model while the transfer of the principal shear stress is accounted for in the boundary layer of the counter-pressure gradient in the near-wall region, and the Bradshaw-proposed assumption of the proportionality of the principal shear stress is introduced to the turbulence kinetic energy into the definition of vortex viscosity. This leads to improved prediction accuracy in computational simulations. (Ma et al., 2021; Zeng et al., 2023). Due to the aforementioned advantages, the shear stress transport turbulence model has been extensively used to investigate the internal flow of the compressor and has experimentally proven to be of high accuracy. (Zhao et al., 2019; Ju et al., 2021; Tang et al., 2021; Hosseinimaab & Tousi 2022).

The expression for the tensor in the SST model is as follows:

$$\rho\frac{\partial(k)}{\partial t} + \rho\frac{\partial}{\partial x_j}(u_i k) = \frac{\partial}{\partial x_j}\left[\left(\mu + \frac{\mu_i}{\sigma_k}\right)\frac{\partial k}{\partial x_j}\right] + G_k - Y_k + S_k \tag{5}$$

$$\rho\frac{\partial(\omega)}{\partial t} + \rho\frac{\partial}{\partial x_j}(u_i \omega) = \frac{\partial}{\partial x_j}\left[\left(\mu + \frac{\mu_i}{\sigma_k}\right)\frac{\partial \omega}{\partial x_j}\right] + G_\omega - Y_\omega + D_\omega + S_\omega \tag{6}$$

where i and j represent the tensor symbols. k is the turbulence kinetic energy, m^2/s^2. ρ denotes the density, kg/m^3. t represent the time of fluid flow, s.

2.3 Model of Centrifugal Compressor

Figure 1 illustrates the computational model. The model encompasses the entire assembly of the centrifugal compressor, comprising the inlet pipe, semi-open centrifugal impeller, vaned diffuser, volute, and outlet pipe. Table 1 displays the key geometrical parameters of the centrifugal compressor. The compressor operates at a rotation rate of 32,638 rpm, with a designed mass-flow rate of 1.77 kg/s. Ideal gas is used as the medium in all numerical simulations. The inlet pipe and outlet pipe are gradually expanding.

Table 1 demonstrates the geometrical parameters of the centrifugal compressor components. The semi-open centrifugal impeller consists of 8 main blades and 8 splitter blades and is a backward impeller. The vane diffuser consists of 11 blades.

2.4 Grid Generation and Independent Test

The computational fluid domain is constructed using ICEM CFD and Turbogrid software. Figure 2 displays the computational domain grid, where the structural grids of the impeller and airfoil diffuser are generated by Turbogrid, and the structural grids of the inlet pipe, volute, and outlet pipe are generated by ICEM CFD. The overall grid quality, maximum skewness, and minimum orthogonal quality meet the criteria of accurate numerical calculations. In this paper, the global structured grid is used in all numerical simulations.

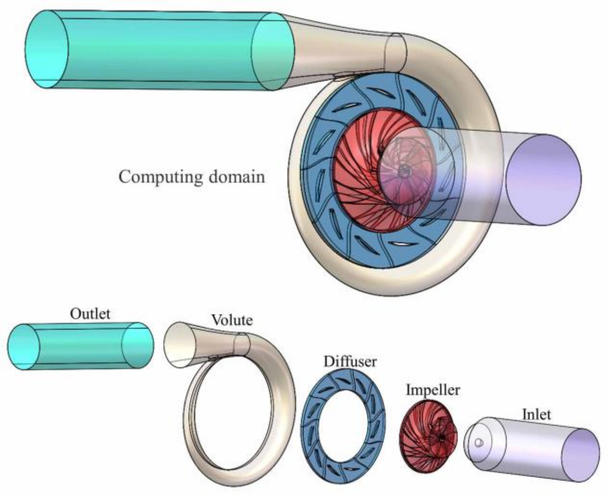

Fig. 1 Geometry of the centrifugal centrifugal compressor

Table 1 Main geometrical parameters of the centrifugal compressor

Parameters	Value
Design rotating speed（r/min）	32638
Design mass flow rate（kg/s）	1.77
Main blades of the impeller	8
Splitter blades of impeller	8
blades of diffuser	11
Diameter of impeller inlet D_1 (mm)	146.9
Diameter of impeller outlet D_2 (mm)	264.8
Width of impeller outlet b_2 (mm)	11.65
Diffuser diameter D_3 (mm)	432
Blade installation angle of the inlet on hub side β_{B1} (°)	64.8
Blade installation angle of the inlet on shroud side β_{B1} (°)	22.8
Blade installation angle of the outlet β_{B2} (°)	51.0
Design inlet tip clearance (mm)	1

Specifically, the grid of the impeller blades was further refined to ensure accurate numerical calculations.

For the flow field of centrifugal compressors, it is required to locally modify the near wall grid to guarantee that the value of y plus meets the accuracy criteria required for the SST turbulence models (Ekradi & Madadi 2020; Liu et al., 2022), So the height of the first layer of the grid in this work is 5×10^{-6} m. In this paper, the inlet tip clearances within a relative clearance of 5%-10% are implemented based on engineering experience and the deformation impact of the blade (Schleer et al., 2008) (the ratio between clearance height and impeller outlet width b_2) of 0.6mm,0.8mm,1mm, and 1.2mm respectively.

A compressor model with an inlet tip clearance of 1 mm is utilized to access grid independence in this work. The computational domain is divided into five different configurations. The polytropic efficiency and the total pressure ratio of the centrifugal compressor are obtained by numerical simulations. Figure 3 displays the validation of grid independence based on the pressure

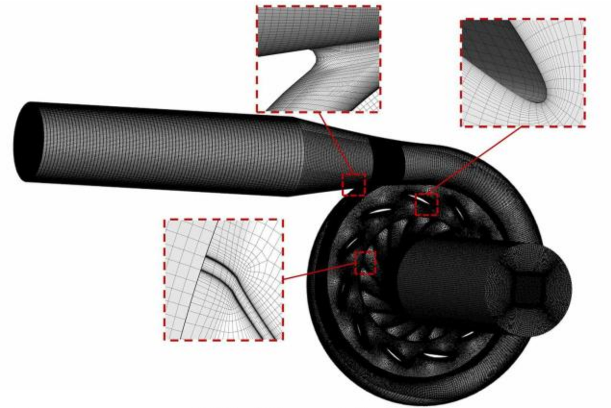

(a) Grid of the centrifugal compressor

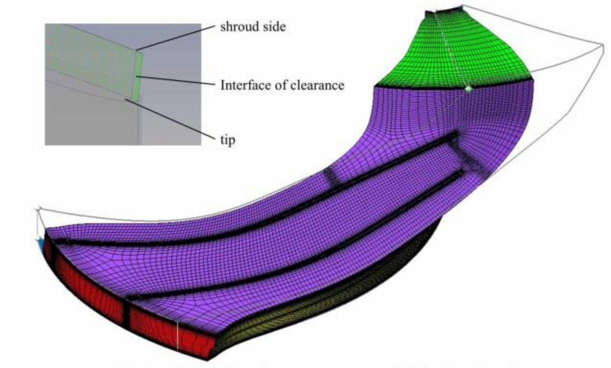

(b) Grid of the Single passage and blade tip clearance

Fig. 2 Overall grid division diagram of the centrifugal compressor

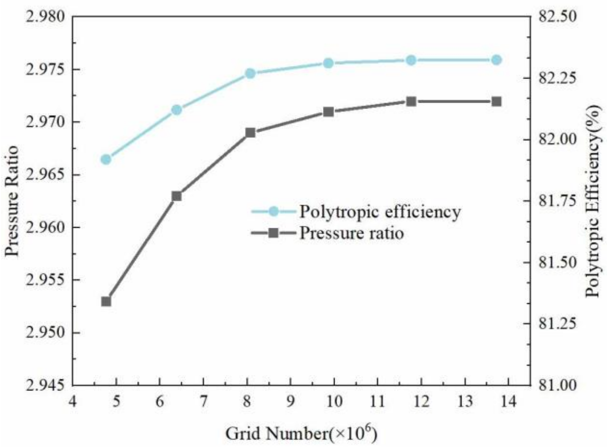

Fig. 3 Validation of grid independence of the centrifugal compressor

ratio and efficiency of the centrifugal compressor. As can be seen from Fig. 3, the difference in pressure ratio and polytropic efficiency is less than 0.1% when 8,000,000 grids are utilized. Based on the above discussion, the number of grids for the computational model is set to 8,000,000 in this study.

2.5 Solution Setup and Boundary Condition

In this paper, the ANSYS CFX 2021R1 is performed to numerically calculate the pressure ratio and efficiency and internal complex flow of a centrifugal compressor.

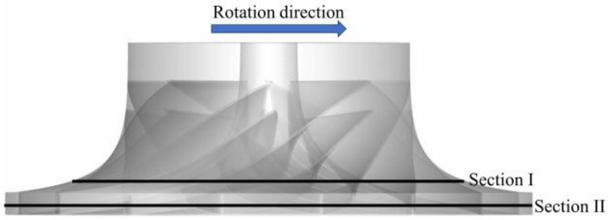

Fig. 4 Location of the impeller section

The solution setup and boundary conditions of the centrifugal compressor are as follows: The total temperature and total pressure at the inlet are specified as 293 K and 98 KPa, respectively. A reference pressure of 0 Pa and a mass flow rate of 1.77 kg/s at the outlet are applied. The total energy is accounted for in the simulation. The SST turbulence model is utilized with an automated wall function for managing wall treatment. All walls are implemented as no-slip walls. The fixed rotor approach (Frozen Rotor) is utilized for the interface with a rotating speed of 32,638 rpm in the impeller region, including the interface between the inlet pipe and the semi-open centrifugal impeller, the semi-open centrifugal impeller, and the vaned diffuser. In general, the residual is less than 1×10^{-5}, and the difference between the inlet and outlet mass flow rates is less than 0.1%.

3. NUMERICAL RESULTS AND DISCUSSION

3.1 Steady Internal Flow of Centrifugal Compressor

3.1.1 Effect of ITC on the Internal Complex Flow of Centrifugal Compressors

Figure 4 shows section I at the 0.8 streamwise (chord length) of the impeller and section II at the half height at the outlet of the centrifugal impeller.

Figure 5 depicts the pressure distributions at the tip of cross-section I. It can be observed that at ITC = 0.6 mm, a significant region of high-pressure is evident at the blade tip near the pressure side (PS), indicating that tip-leakage flow primarily results from the difference in pressure between the PS and suction side (SS), with significant backflows occurring in this area. The size of region A is gradually reduced due to the increase of the inlet tip clearance (ITC). The reduction can be attributed to the tip leakage flow's (TLF) more extensive disruption of the mainstream, which promotes stronger energy in mainstream diffusion. As a result, there is a noticeable decrease in the difference in pressure between the PS and SS at the tip of the blade.

Figure 6 indicates the velocity distributions at the tip of cross-section I. It is evident from Fig. 6 that a high-velocity region is present at the tip of the blade near the SS at ITC = 0.6 mm. The size of this region progressively grows with increasing ITC, indicating a gradual decrease in fluid flow resistance at the tip and an increase in tip leakage flow (TLF). Furthermore, the mixing between mainstream and TLF intensifies in this region.

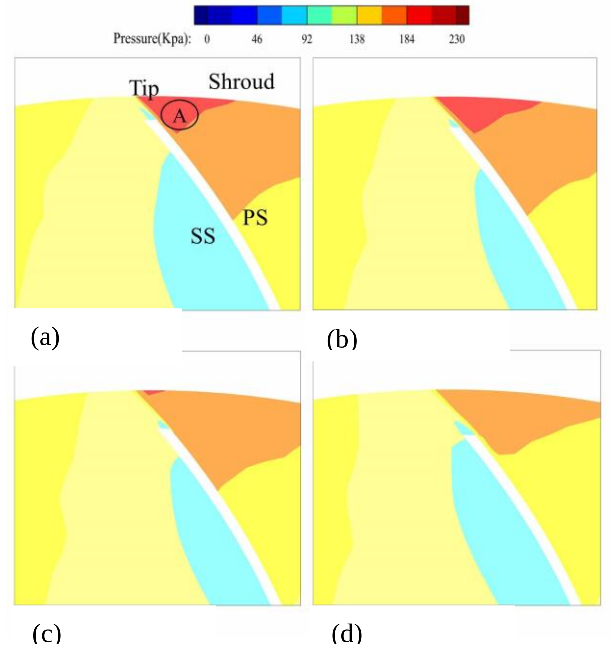

Fig. 5 Comparison of pressure distributions at the 0.8 streamwise of the blade (section I):(a) ITC=0.6mm, (b) ITC=0.8mm, (c) ITC=1mm, (d) ITC=1.2mm

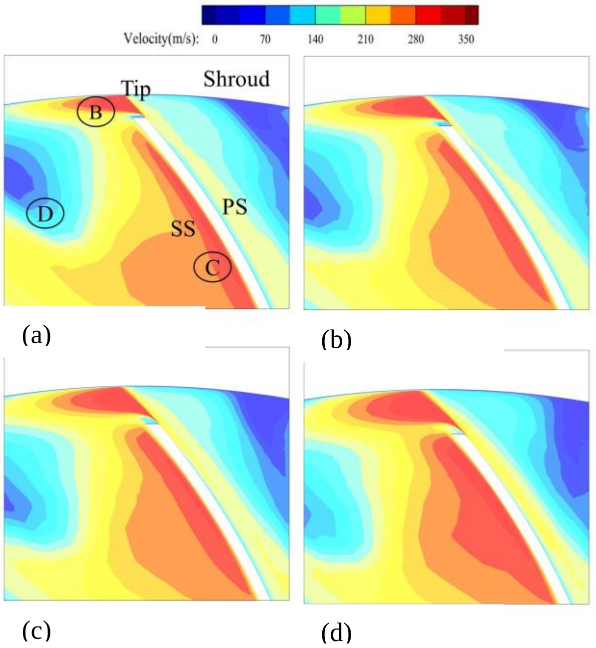

Fig. 6 Comparison of velocity distributions at the 0.8 streamwise of the blade (section I):(a) ITC=0.6mm, (b) ITC=0.8mm, (c) ITC=1mm, (d) ITC=1.2mm.

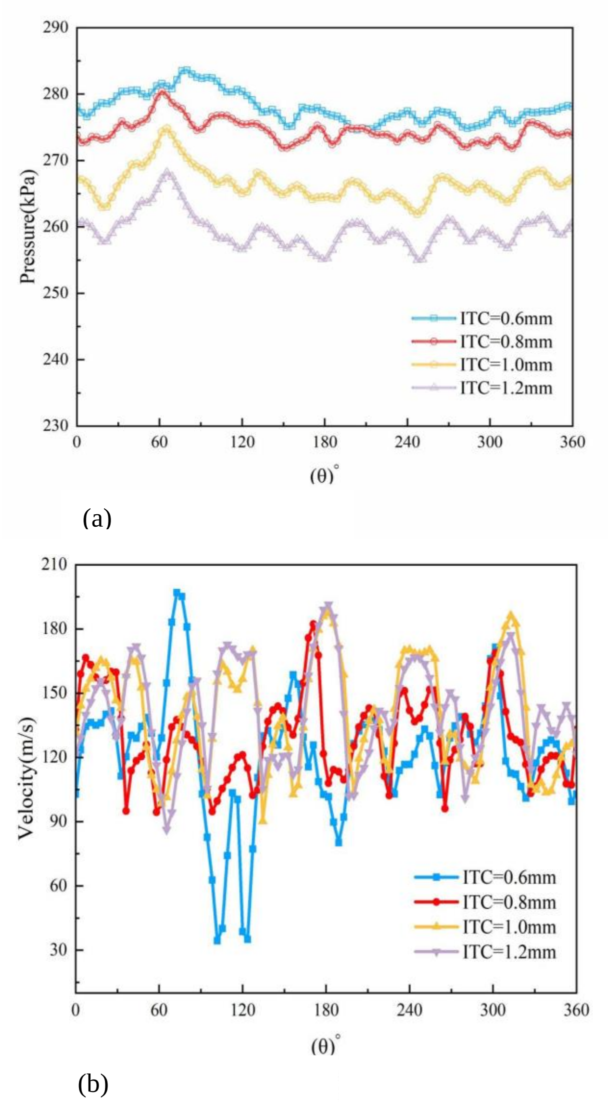

Fig. 7 Pressure & velocity distributions at the 0.8 streamwise and 0.99 span of the blade:(a) Pressure distributions(b) velocity distributions

Figure 7 displays the pressure and velocity distributions of the blade at 0.8 streamwise (chord length) and 0.99 spans (blade height). With increasing ITC, the scale and severity of the TLF, as well as the mixing with the mainstream, increase. This is evidenced by the pressure reduction at the tip. In Fig. 7b, a notable velocity change occurs at ITC = 0.6 mm with a low-velocity region emerging between 90° and 120°, where vortex and backflow may occur. As the ITC increases, the resistance of fluid flow weakens, the low-velocity region disappears, and velocity fluctuation decreases at the tip, indicating a more balanced difference of pressure between the PS and SS and improved flow field uniformity. The mean pressure and velocity values demonstrate that the change at the top of the blade increases and then decreases with increasing ITC.

Figure 8 shows the pressure distribution in Section II. In Fig. 8, it is obviously seen that a large radial gradient of pressure mainly appears between the volute, diffuser, and impeller at ITC = 0.6 mm. With increasing ITC, the gradient of pressure gradually decreases and the area of the low-pressure region increases between the diffuser and the volute, which reveals that the resistance of fluid flow obviously decreases with increasing ITC. The increasing TLF enters the narrow blade passage with the high-speed rotating impeller, which induces more separation flows, secondary flows, and clearance vortices with this phenomenon being particularly pronounced at large ITC.

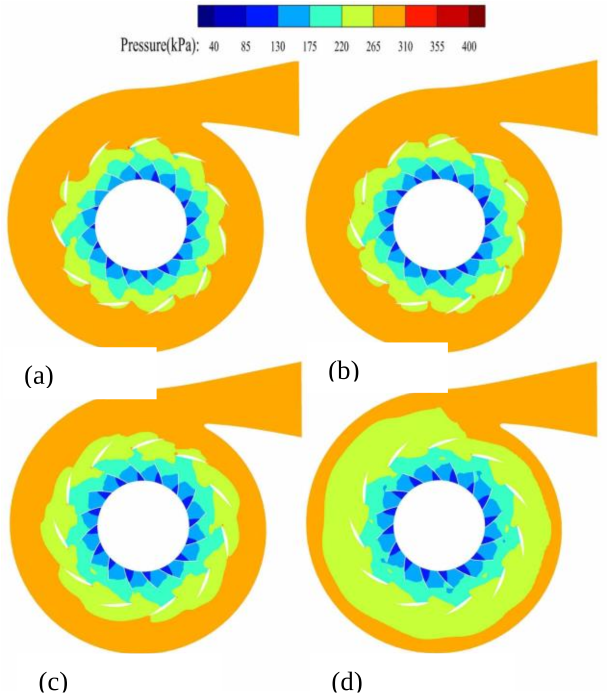

Fig. 8 Comparison of pressure distributions at the middle section of the impeller outlet (section II): (a) ITC=0.6mm, (b) ITC=0.8mm, (c) ITC=1mm, (d) ITC=1.2mm

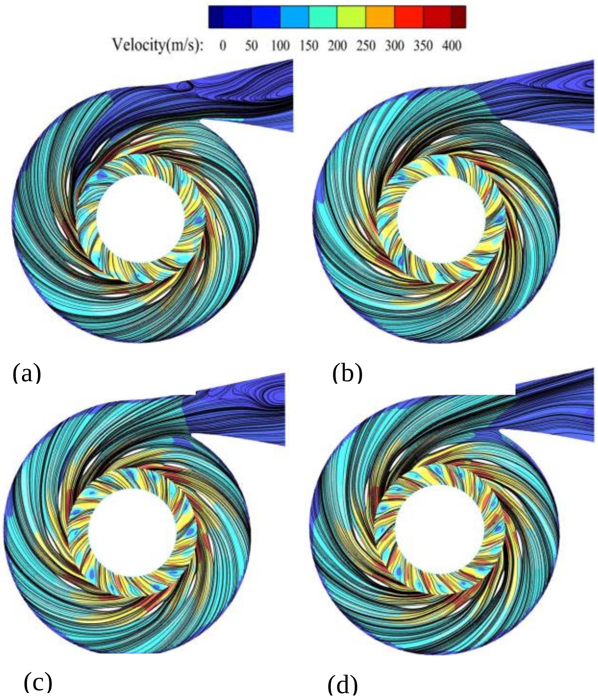

Fig. 9 Comparison of velocity and streamline distributions at the middle section of the impeller outlet (section II) and four inlet tip clearances

(a) ITC=0.6mm, (b) ITC=0.8mm, (c) ITC=1mm, (d) ITC=1.2mm

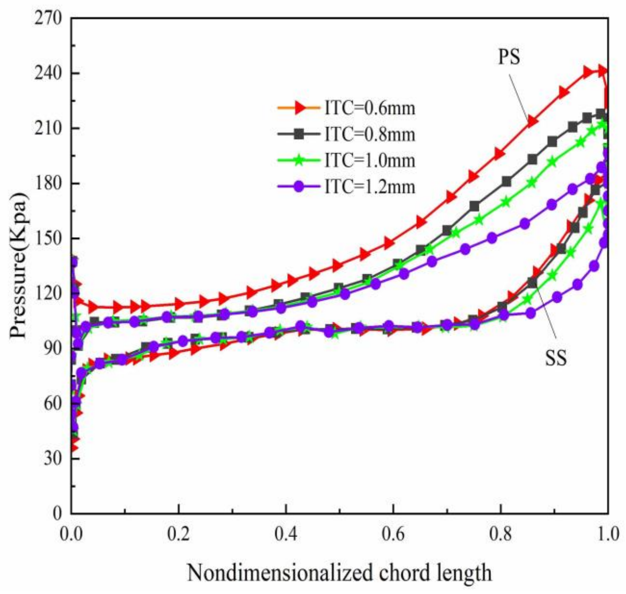

Fig. 10 Relationship between inlet tip clearance and pressure

Figure 9 indicates the velocity contour and streamline distributions in Section II. A significant velocity gradient is observed between the volute, diffuser, and impeller at ITC = 0.6 mm. Numerous vortices form at the volute outlet due to high fluid flow resistance. As the ITC increases, the deflection angle of the streamline and the velocity of PS gradually decrease at the tip. Eventually, the low-velocity vortices vanish at the volute outlet. This is due to the resistance of fluid flow decreasing with increasing ITC, a decrease in pressure gradient between the volute, diffuser, and impeller. Consequently, the fluid flow downstream becomes more uniform, supporting the physical mechanism for expanding the operation range of the centrifugal compressor.

Figure 10 describes the static pressure distribution for the four ITCs on 0.9 span at the rated operating conditions. The horizontal coordinates represent the non-dimensional blade position in the flow direction (chord length), while the vertical coordinates represent the magnitude of the blade loads. As illustrated in Fig. 10, it is obviously seen that the pressure distribution at the LE of the tip is minimally affected by the ITC. However, the pressure decreases noticeably from the middle to the TE of the blade with increasing ITC. This pressure change is more pronounced on the PS compared to the SS, resulting in a larger difference in pressure between the PS and SS, indicating a higher load on the blade. As ITC grows, there is a decreasing pressure difference between PS and SS, indicating reduced blade loading and increased impeller safety. Moreover, the relationship between blade tip load and ITC size is not linear.

The *Q*-criterion is a key analytical tool in fluid mechanics, particularly useful for studying flow separation phenomena and vortex dynamics. It is commonly used in computational simulations to pinpoint regions with high vorticity, shedding light on complex flow structures like separation vortices. By identifying areas where the *Q*-criterion exceeds set thresholds, researchers can analyze the origin, development, and

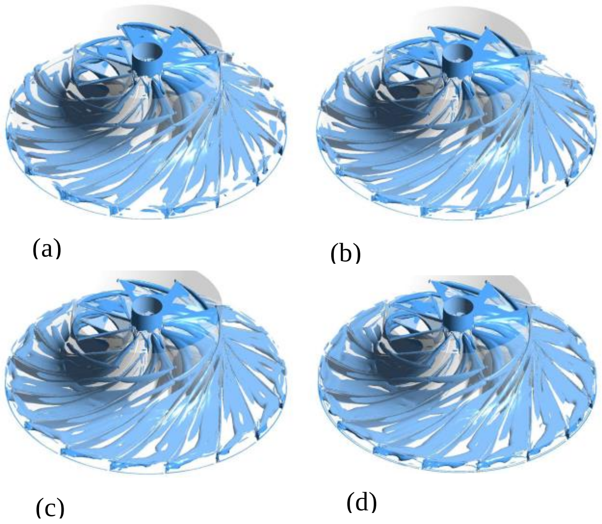

Fig. 11 Comparison of TLV characteristics(*Q*-criterion) at various inlet tip clearance:(a) ITC=0.6mm, (b) ITC=0.8mm, (c) ITC=1mm, (d) ITC=1.2mm

impact of vortices on the overall flow pattern in detail (Chen et al., 2022; Li et al., 2023; Zheng et al., 2024).

The equation for the *Q*-criterion is shown as follows:

$$\Omega_{ij} = \frac{1}{2}\left(\frac{\partial u_i}{\partial x_j} - \frac{\partial u_j}{\partial u_i}\right) \tag{7}$$

$$S_{ij} = \frac{1}{2}\left(\frac{\partial u_i}{\partial x_j} + \frac{\partial u_j}{\partial u_i}\right) \tag{8}$$

$$Q = \frac{1}{2}\left(\|\Omega\|^2 - \|S\|^2\right) \tag{9}$$

where Ω_{ij} represents the vorticity tensor and S_{ij} represents the strain-rate tensor.

A positive *Q* value indicates regions mainly influenced by vorticity, indicating significant rotational motion. Conversely, negative *Q* values indicate regions where strain rates or viscous stresses dominate, suggesting regions characterized by deformation or viscous dissipation. The precise visualization and characterization of vortex structures within the flow domain are effectively captured by using iso-surfaces of the *Q*-criterion, providing profound insights into underlying flow mechanisms.

Figure 11 represents the tip leakage vortex (TLV) of the four ITCs in the semi-open centrifugal impeller. Based on the advantages of the *Q*-criterion mentioned above, the TLV core in this paper is identified using the *Q*-criterion. After comparative analysis, the vortex evolution is clearly periodic when the *Q* value $=1.2906\times10^{8}$ s^{-2}(level=0.003). Therefore, the *Q* value of 0.003 was selected to capture the subtle vortex evolution. The TLV's three-dimensional helical formation is attributed to entrainment with the incoming flow and pressure differentials between the PS and SS of the impeller blade, whereas the mixing of the mainstream and TLF is the primary cause of flow distortions. As ITC increases, the TLV strengthens, particularly downstream of the flow passage, indicating heightened TLF and an increased degree of disruption to the mainstream downstream.

Figure 12 displays the distribution of turbulence kinetic energy (TKE) within the semi-open centrifugal impeller on different circular sections (0.6*R*, 0.8*R*, and 0.99*R*). The fluid entering the flowing passage is accompanied by a significant loss of turbulent energy, as seen in Fig. 12, predominantly occurring at the top of the suction surface. Moreover, there is an observed gradual escalation of this dissipation along the direction of flow.

Figure 13 indicates the streamlines of the mainstream in three sections at different inlet tip clearances. A portion that is vertical to the flow direction shows how TLF affects the mainstream. The TLF has little influence on the mainstream up to the 60% position of the flow direction, as the four figures to the left (position 1) demonstrate. At Position 2 (0.8 streamwise), the TLF has the most significant influence. The streamline in the middle and trailing edge of the blade passage becomes increasingly distorted, indicating a stronger impact of tip clearance with increasing clearance size. Consequently, the distorted streamline shifts toward the top-left and bottom-right, respectively, leading to an increase in velocity in Region 1 and a decrease in Region 2. The four figures on the right depict the gradual weakening of the TLF's influence on the mainstream after 0.99 streamwise. Meanwhile, the streamline distortion at region IV of PS becomes more pronounced, and velocities at regions III and IV of PS increase with increasing ITC. These observations further emphasize that the TLF predominantly affects the middle region to the TE of the flow passage, while the LE experiences minimal impact.

3.1.2 Aerodynamic performance of numerical simulations

The TLF from the inlet tip will enter the narrow flow passage with the high-speed rotating impeller (32638 rpm), inducing more separation flow, secondary flow, and clearance vortex, thus reducing the aerodynamic performance of the centrifugal compressor. Figure 14 denotes the aerodynamic performance of the centrifugal compressor at four inlet tip clearances (ITCs). The curves indicates that ITC significantly influences the performance of the centrifugal compressor: as ITC rises, the total pressure ratio drops, polytropic efficiency rises and subsequently drops, and the efficiency peak shifts toward a low mass flow rate. Notably, the operating range of the centrifugal compressor expands with increasing ITC. At design conditions (1.77 kg/s), the pressure ratio decreases by 0.7%, and the polytropic efficiency drops by 0.1% when ITC rises from 0.6 mm to 0.8 mm. When the ITC is raised from 0.8 mm to 1 mm, the polytropic efficiency decreases by 3.1%, and the total pressure ratio decreases by 2.0%. Similarly, with an increase from 1 mm to 1.2 mm, the total pressure ratio drops by 2.0%, and the polytropic efficiency drops by

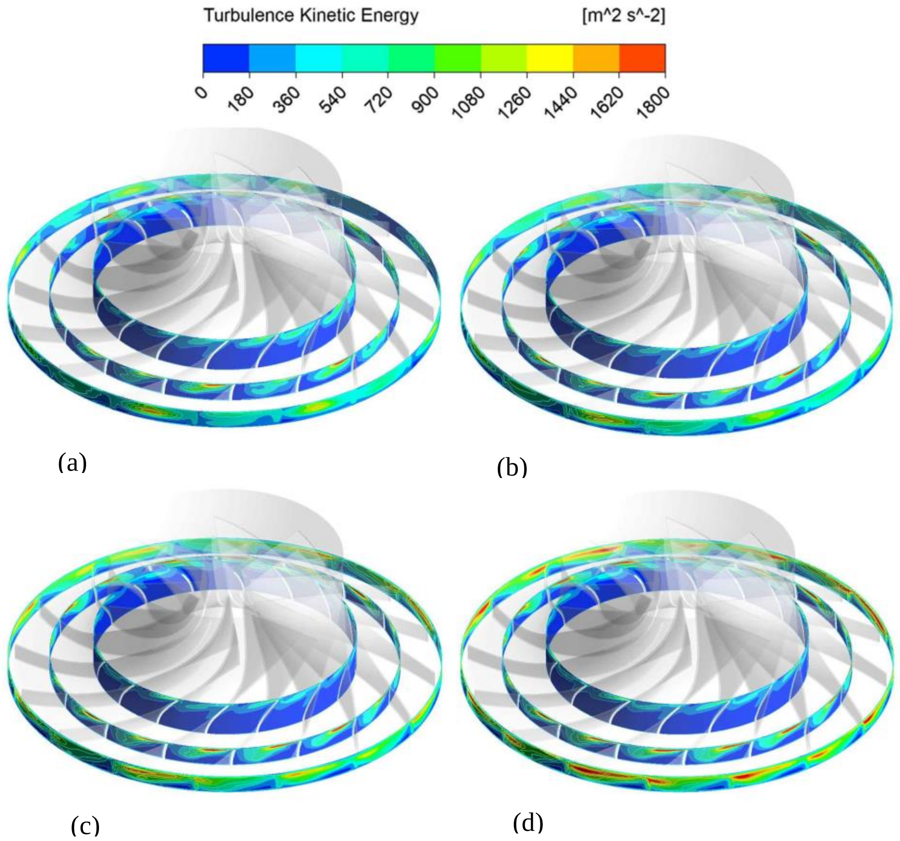

(a) (b)

(c) (d)

Fig. 12 Turbulent kinetic energy distribution on the different circle sections in the impeller: (a) ITC=0.6mm, (b) ITC=0.8mm, (c) ITC=1mm, (d) ITC=1.2mm

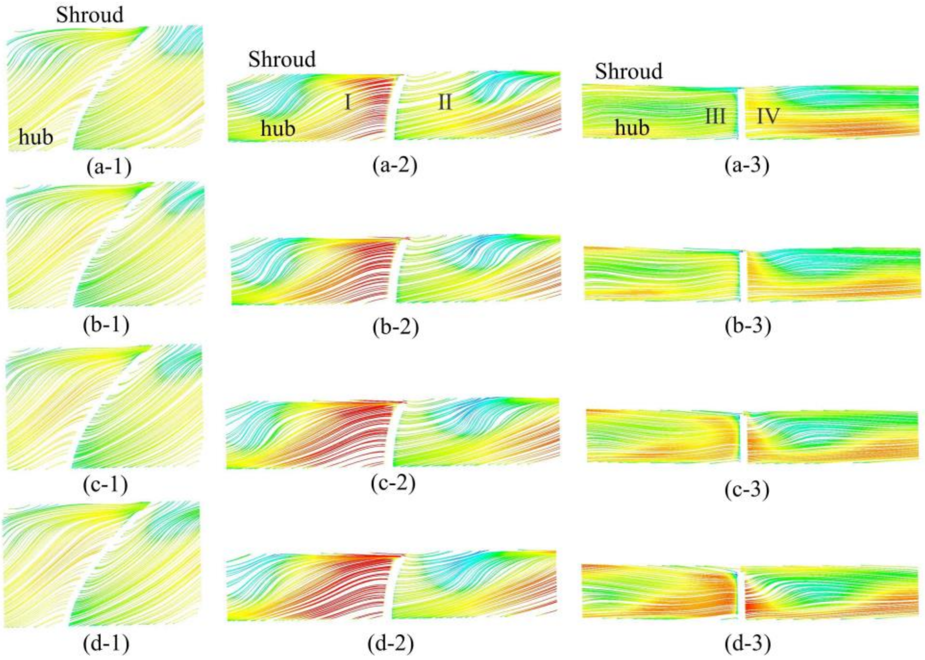

Fig. 13 Mainstream streamlines with different flow cross sections at 4 tip clearance: (a) ITC=0.6mm, (b) ITC=0.8mm, (c) ITC=1mm, (d) ITC=1.2mm

1.38%. In line with the findings of Mao and Xiang (Mao & Liu 2017; Xiang et al., 2019), an increase in the tip clearance consequently reduces the aerodynamic performance of the compressor. Furthermore, a notable nonlinear relationship is obtained between them. Compared to low mass flow rate conditions, the performance deteriorates more rapidly at high mass flow rate conditions.

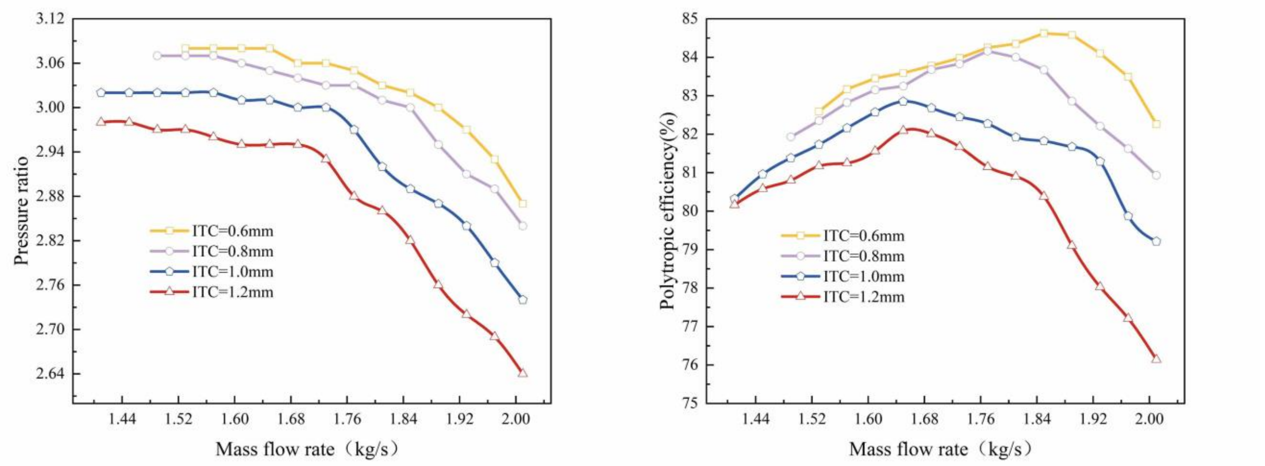

(a) The relationship between pressure ratio and mass flow rate (b) The relationship between polytropic efficiency and mass flow rate

Fig. 14 Aerodynamic performance of the centrifugal compressor

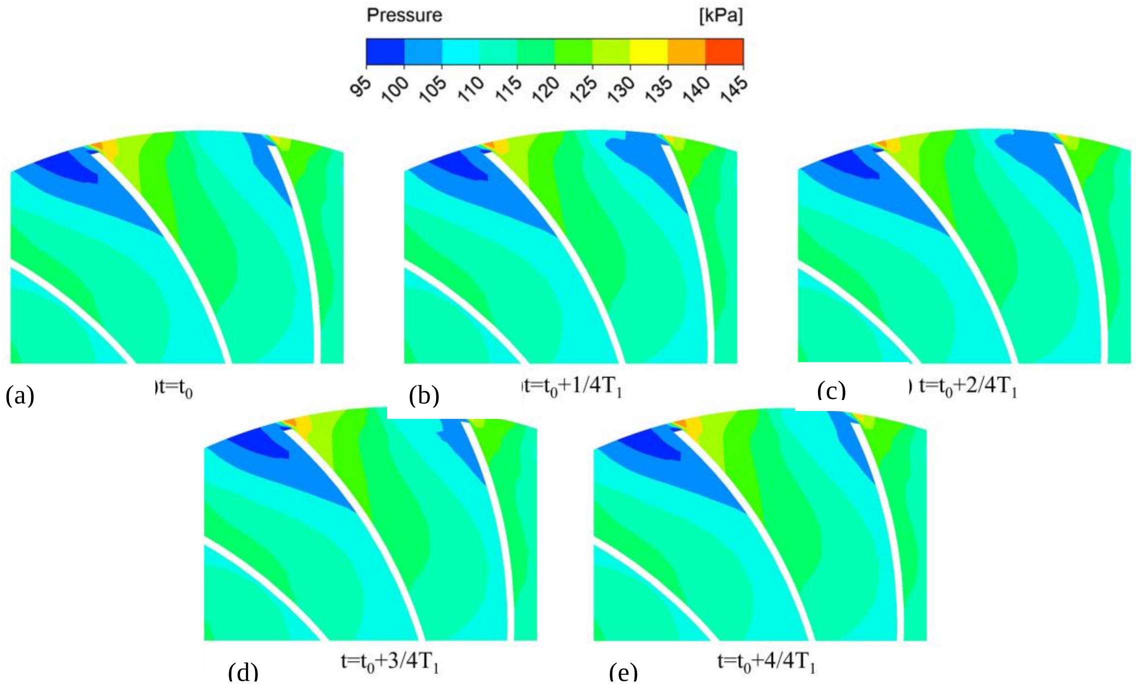

Fig. 15 Pressure distributions at the 0.8 streamwise of the blade (section I)

3.2 Unsteady Flow of Centrifugal Compressor

In this subsection, numerical simulations will be utilized to analyze the internal complex flow within a compressor with four ITCs at rated operating conditions. For the unsteady simulation, the time step was chosen to be the time required to rotate the centrifugal impeller by 2° and was calculated to be 1.0213×10^{-5} s. To ensure numerical simulation accuracy, computational results from the centrifugal compressor after ten revolutions are chosen for data analysis, T_1 denotes the time for one revolution, and t_0 represents ten revolutions of the impeller.

Figure 15 shows the pressure distributions in Section I at rated conditions with the designed ITC. It is evident from Fig. 15 that the low-pressure area near the SS of the impeller blade is smaller at $t = t_0$. However, at $t = 2T_1/4$, the area of low pressure notably increases, indicating a gradual rise in TLF. Consequently, the mainstream is more disturbed by the TLF, resulting in more prominent secondary and separated flows at the SS, which is well consistent with the previous work. (Zhu et al., 2020). By $t=4T_1/4$, the pressure distribution in the flow passage closely resembles that at t_0. The TLF exhibits regular periodic motion.

Figure 16 depicts the streamlines at 0.9 span for one revolution at rated conditions and designed ITC. As described in Fig. 16, detailed flow disturbances caused by TLF are clearly visible. The tip-leakage flow induces separation and secondary flows, primarily occurring at the tip of the pressure side (PS). The streamline in Region II intersects to generate a leaking vortex at t=t0, while the streamline in Region I is uniform. The fluid field undergoes significant changes in this region.

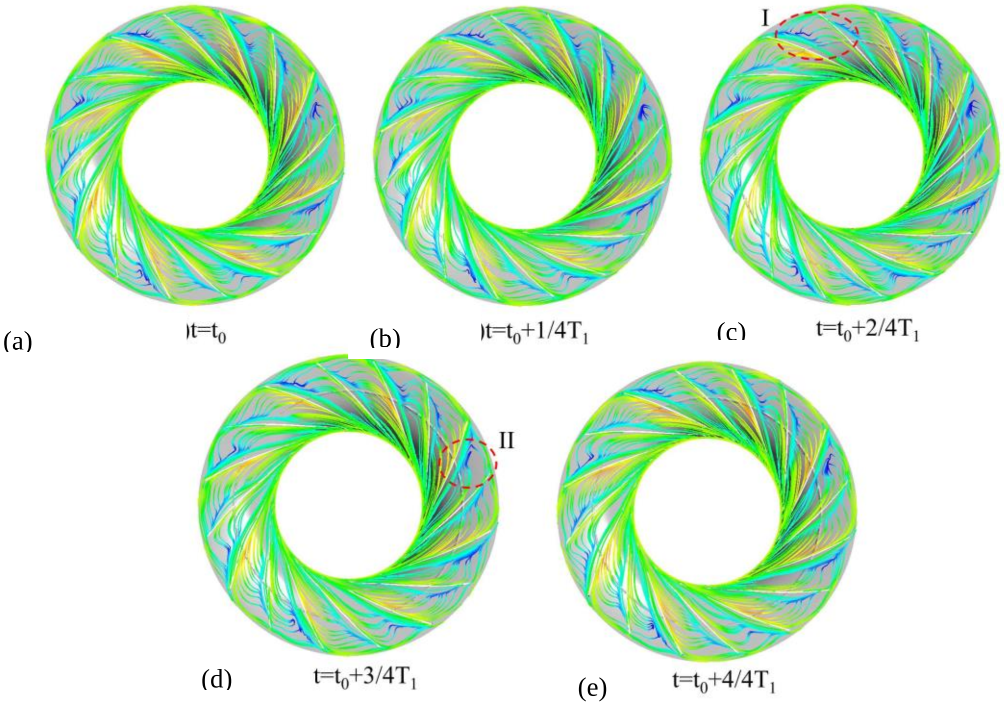

Fig. 16 Spatiotemporal evolution characteristics of the streamlines for the design inlet tip clearance (1mm) at rated operating conditions

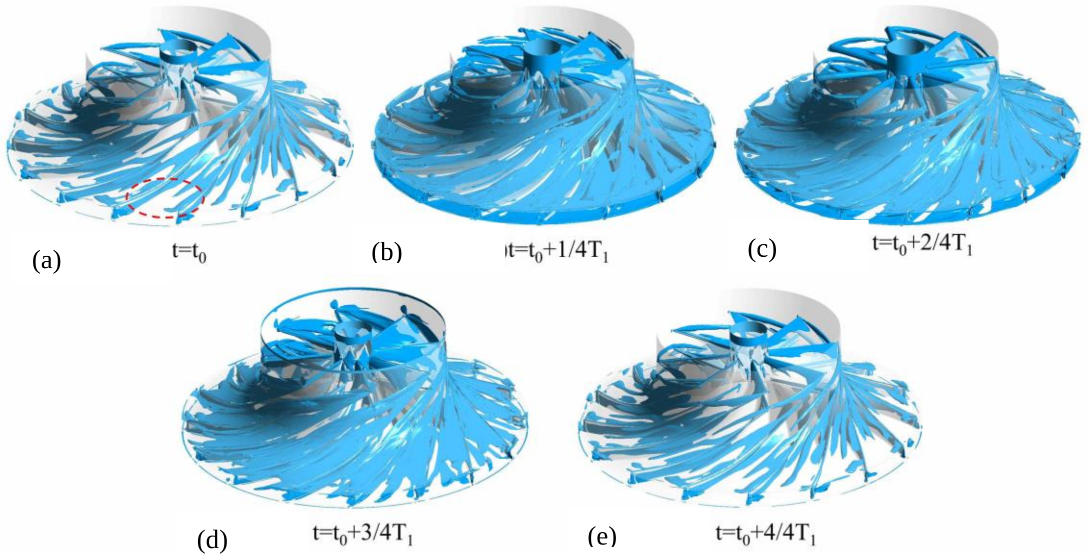

Fig. 17 Spatiotemporal evolution of the vortex structures (*Q*-criterion) in the impeller region at ITC=1mm

As time evolves, the streamlines in Region I diminish, and separation flow occurs at t = 2T1/4. The tip-leakage vortex disintegrates at Region II and vanishes at t = 4T3/4. Eventually, the streamlines return to the distribution observed at t = t_0 by t = 4T4/4. These results demonstrate that the evolution of flow development under the designed ITC at rated operating conditions follows the cycle of one rotation of the impeller, which is in good agreement with the previous work (Xu et al., 2022).

Figure 17 illustrates the spatiotemporal evolution of the tip leakage vortex (TLV) structure at rated operating conditions. As revealed by the TLV, large-scale leakage flows, secondary flows, and separation flows from the tip clearance enter the flow passage. At t= t_0, the impeller exhibits less leakage flow and secondary flow, particularly downstream of the flow passage. At $2T_1/4$, there is a sharp increase in leakage and secondary flows at the tip accompanied by the formation of the TLV, filling the downstream passage. At t = $3T_1/4$, the TLF diminishes as the TLV disintegrates and disappears in the middle and downstream of the blade passage. Finally, at t=$4T_1/4$, both the leakage vortex and secondary flow rapidly decrease, and a non-stationary rotation cycle of the TLV is completed. This physical phenomenon is well consistent with previous research (Zamiri et al., 2017).

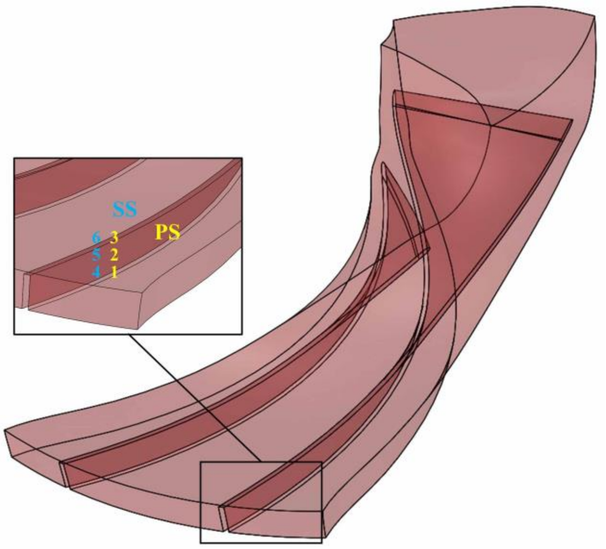

Fig. 18 Location of monitoring points in the impeller passage

Figure 18 illustrates the location of the monitoring points where detailed characteristic measurements were performed during the subsequent work. The monitoring points of the PS and SS are located at 0.2, 0.6, and 0.99 blade height (span) along 80% of the chord length (0.8 streamwise). The unsteady flow characteristics at rated operating conditions are investigated by time-scale pressure and velocity fluctuations.

Figure 19 denotes the pressure fluctuation distribution characteristics of the monitoring point at ITC = 0.6 mm. It is evident that the pressure fluctuation at the monitoring point is unstable. Similar pressure fluctuation characteristics at Points 1 and 4 are captured at the bottom of the impeller, indicating less influence from the TLF at the bottom of the PS and SS. Points 2, 3, 5, and 6 represent pressure fluctuations at the middle and top of the PS and SS, respectively. The average pressures are 170.0, 161.5, and 104.6, 105.3 at ITC = 0.6 mm. The strongest fluctuations always occur in the most intricate region of the vortex in the tip clearance on the PS, which is consistent with previous work (Taghavi-Zenouz, & Eslami 2012).

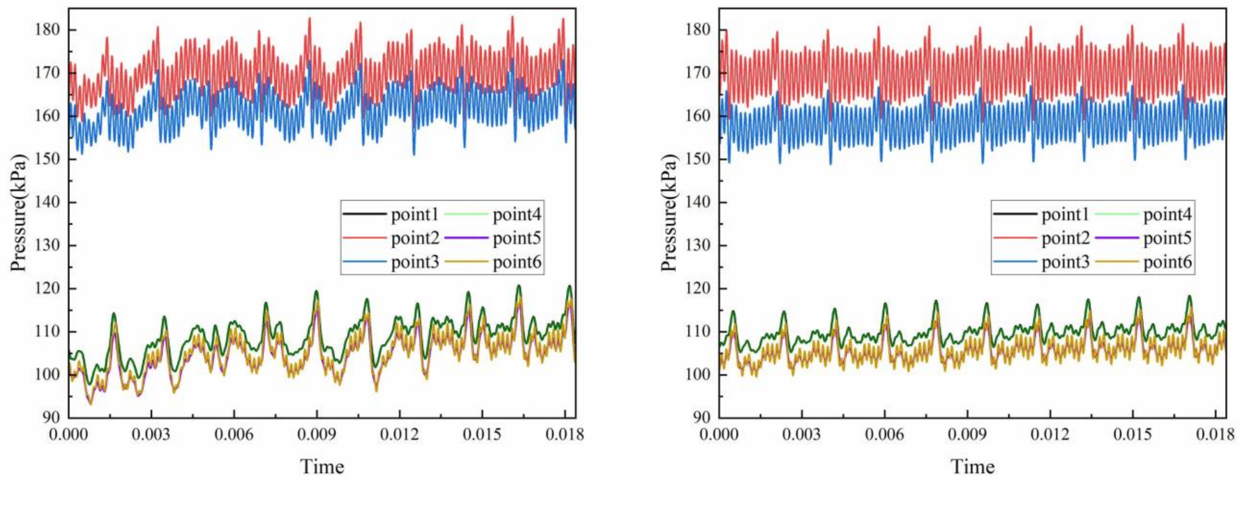

(a) Pressure fluctuation at ITC=0.6mm (b) Pressure fluctuation at ITC=0.8mm

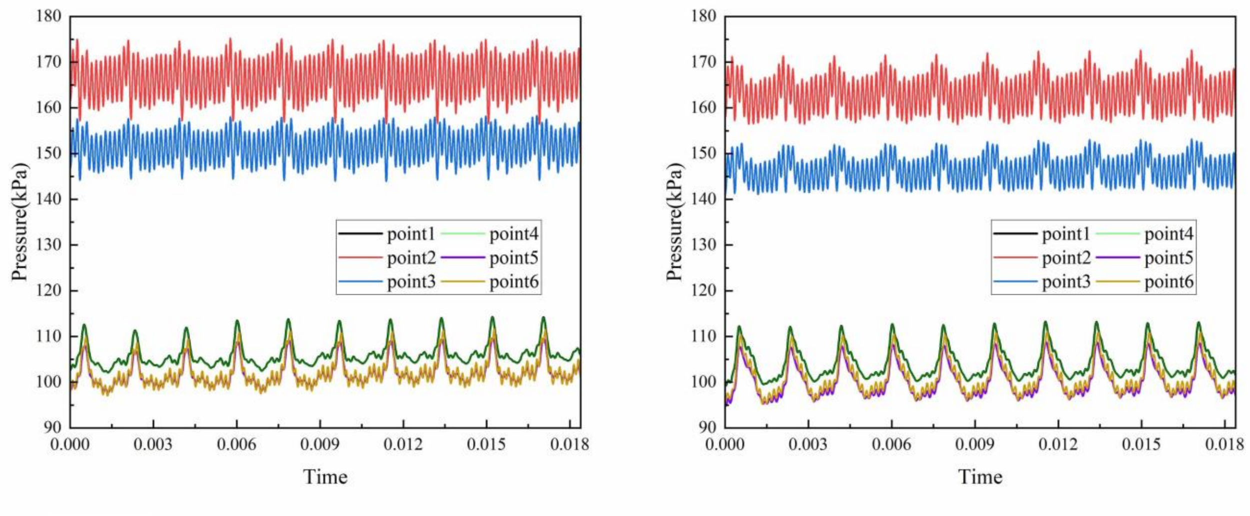

(c) Pressure fluctuation at ITC=1mm (d) Pressure fluctuation at ITC=1.2mm

Fig. 19 Pressure fluctuation distribution characteristics at different inlet tip clearance

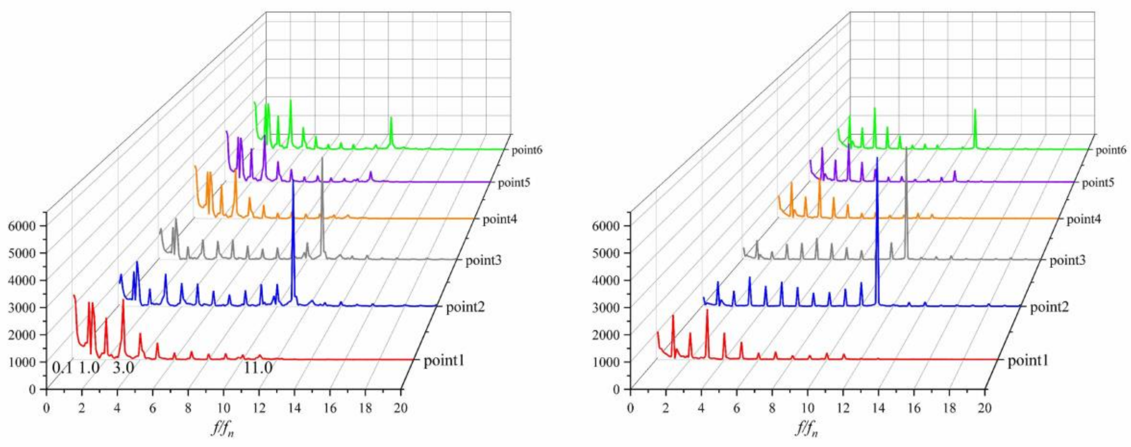

(a) FFT of pressure fluctuation at ITC=0.6mm (b) FFT of pressure fluctuation at ITC=0.8mm

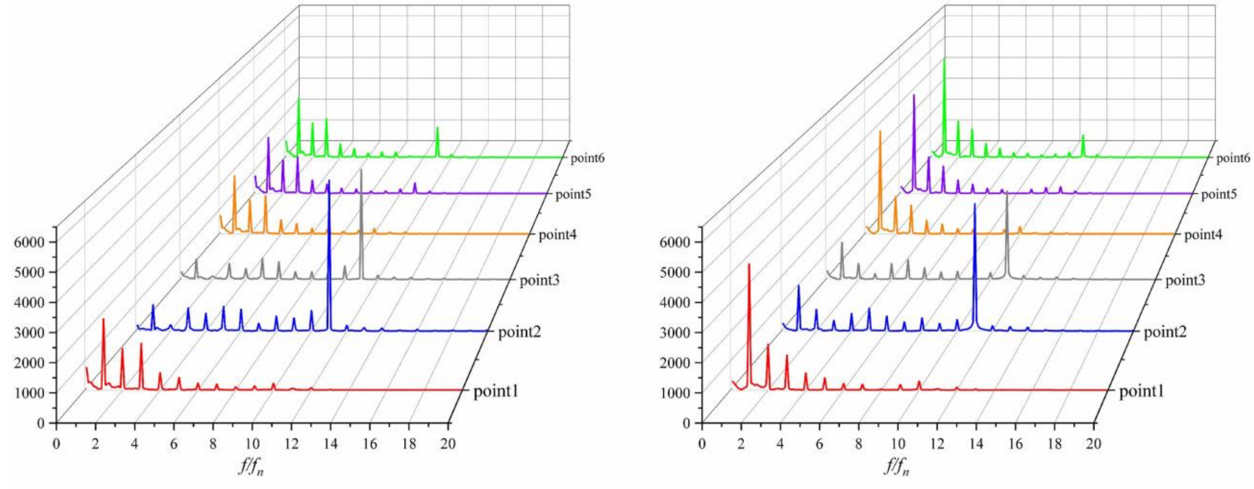

(c) FFT of pressure fluctuation at ITC=1mm (d) FFT of pressure fluctuation at ITC=1.2mm

Fig. 20 FFT of pressure fluctuation at different inlet tip clearance

It is observed that the pressure difference between points 2 and 3 decreases with increasing ITC. The average pressure at the middle and top of PS and SS decreased by 4.0%, 9.3% and 4.3%, 3.9% at ITC = 1.2 mm, indicating an intricacy effect of TLF at the top of the impeller compared to the middle, and the effect on PS was greater than that on SS. These phenomena may result from ameliorating flow resistance and backflow in the tip region with increasing ITC. To better comprehend the influence of ITC on the internal complex flow of semi-open centrifugal impellers, the fast Fourier transform (FFT was carried out at the monitoring points to analyze the spectral characteristics.

Figure 20 displays the FFT of pressure fluctuations at four ITCs. The x-axis represents the value of frequency after dimensionless normalization according to the rotational frequency (*fn* = 543.97 Hz). The y-axis represents the 6 monitoring points near the wall in the flow passage. The z-axis represents the value of the amplitude.

As depicted in Fig. 20, the fluctuation amplitudes differ at the four ITCs, but the frequency characteristics are nearly identical, primarily determined by the blade rotation frequency and its multiples. The frequency distribution at ITC = 0.6 mm shows that there is significant flow resistance at the top of the impeller, with the TLF primarily influencing the middle and top at the PS. At points 1, 4, 5, and 6, 3.0 *fn* dominates, while 11.0 *fn* dominates at points 2 and 3. At ITC = 1.0 mm, the frequency of 1.0 *fn* predominates at points 1, 4, 5, and 6. At ITC = 1.2 mm, the amplitudes at points 1, 4, 5, and 6 sharply rise compared to ITC = 1.0 mm, while those at points 2 and 3 decrease. This suggests that for ITC = 1.2 mm, the tremendous scale of leakage flow causes the PS pressure to drop and the SS pressure to rise noticeably. The analysis of the pressure spectrum indicates a stronger effect of TLF on the middle and top of the PS than on the bottom of the PS and the SS. The scale of the TLF increases progressively with increasing ITC, with its impact on PS flow diminishing and on SS flow intensifying.

Figure 21 describes the velocity fluctuation distribution characteristics of the monitoring points with different ITCs. There appear to be more disordered velocity fluctuations at the 0.6 and 0.9 spans near the SS at ITC = 0.6 mm, indicating that smaller ITCs are more resistant to fluid flow than larger ITCs. The average velocities at the middle and top of the PS and SS are 147.5, 165.3, 294.5, and 317.3 at ITC = 0.6 mm. As ITC increases, the resistance of fluid flow and backflow

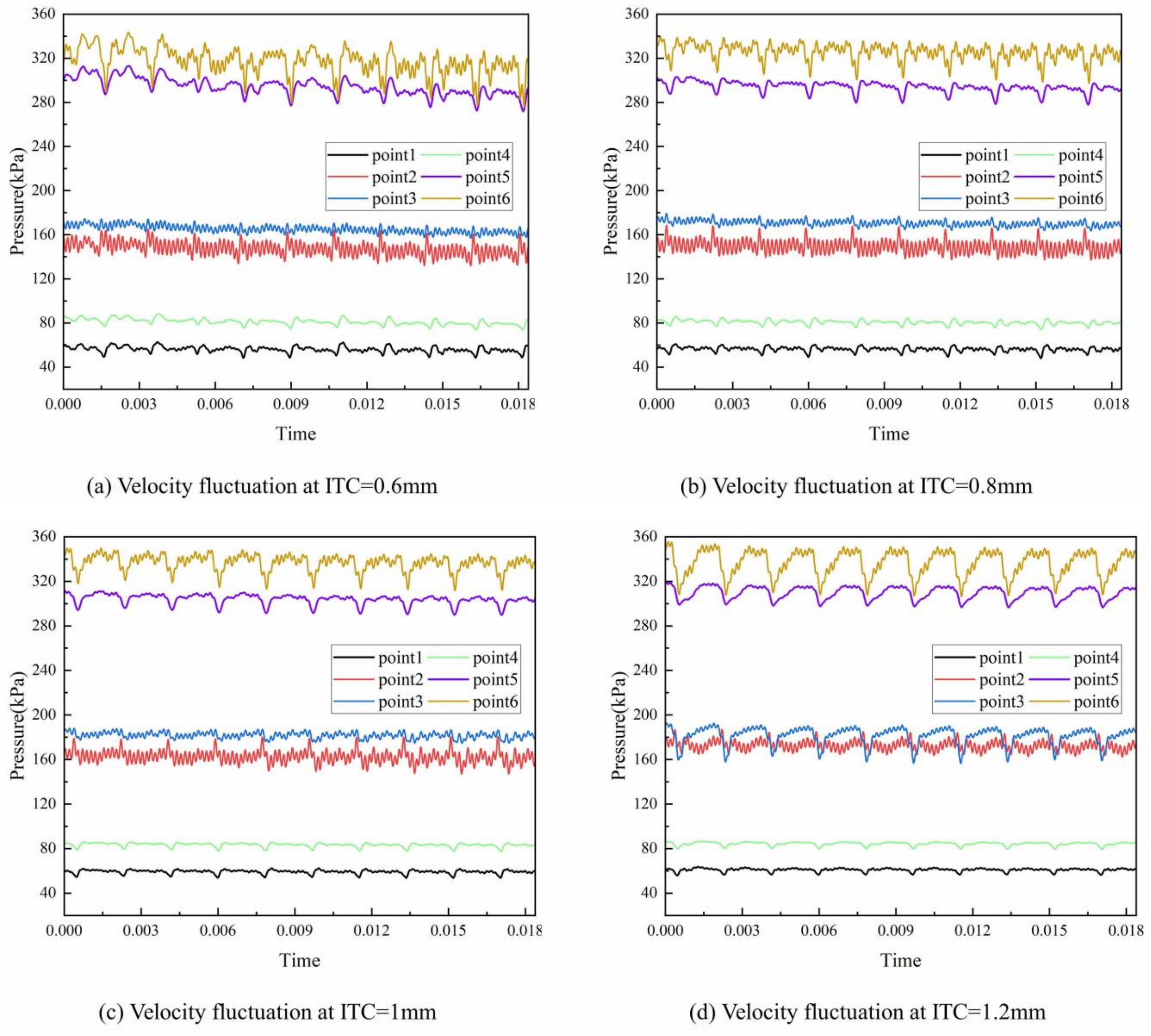

(a) Velocity fluctuation at ITC=0.6mm

(b) Velocity fluctuation at ITC=0.8mm

(c) Velocity fluctuation at ITC=1mm

(d) Velocity fluctuation at ITC=1.2mm

Fig. 21 Velocity fluctuation distribution characteristics at different inlet tip clearance

decreases at the top of the blade, in contrast, the TLV scale increases. Consequently, the velocity fluctuations of SS at 0.6 and 0.9 span become more regular, and the fluctuation curves move upward. The average velocity at the middle and top of PS and SS is reduced by 17.1%, 9.1%, 5.2%, and 6.1%, respectively, at ITC = 1.2 mm, further demonstrating TLF has a more substantial impact on PS than SS. These phenomena further validate the decrease in pressure (Fig. 19).

Figure 22 displays the frequency spectra of velocity pulsations at six monitoring points. The velocity spectrum is less prominent than pressure variations when compared to each other, yet the distribution patterns are similar. The dominant frequency is the rotational frequency of the blade and its octave. High-frequency fluctuations are observed at monitoring points 2 and 3, while low-frequency fluctuations occur at monitoring points 1, 4, 5, and 6 for ITC = 0.6mm. The main reason for the dominant frequency can be seen in the analysis of Fig. 20.

4. CONCLUSIONS

The present numerical simulation study investigated the steady and unsteady internal complex flow characteristics of a centrifugal compressor with different ITCs. The detailed conclusions are as follows:

First of all, the fluid flow resistance decreases with an increase in inlet tip clearance (ITC). Thus, more tip leakage flow (TLF) disturbs the mainstream more intensely, which causes the mainstream energy to diffuse. Larger ITCs result in more noticeable alterations in the flow field and a significant reduction in the pressure gradient between the volute, diffuser, and impeller. This improves the uniformity of the flow field within the compressor and causes the low-speed vortex near the outlet of the volute to vanish. The above phenomenon confirms the physical mechanism behind expanding the operational range of the centrifugal compressor. Furthermore, the size of the ITC notably affects the aerodynamic performance of the centrifugal compressor.

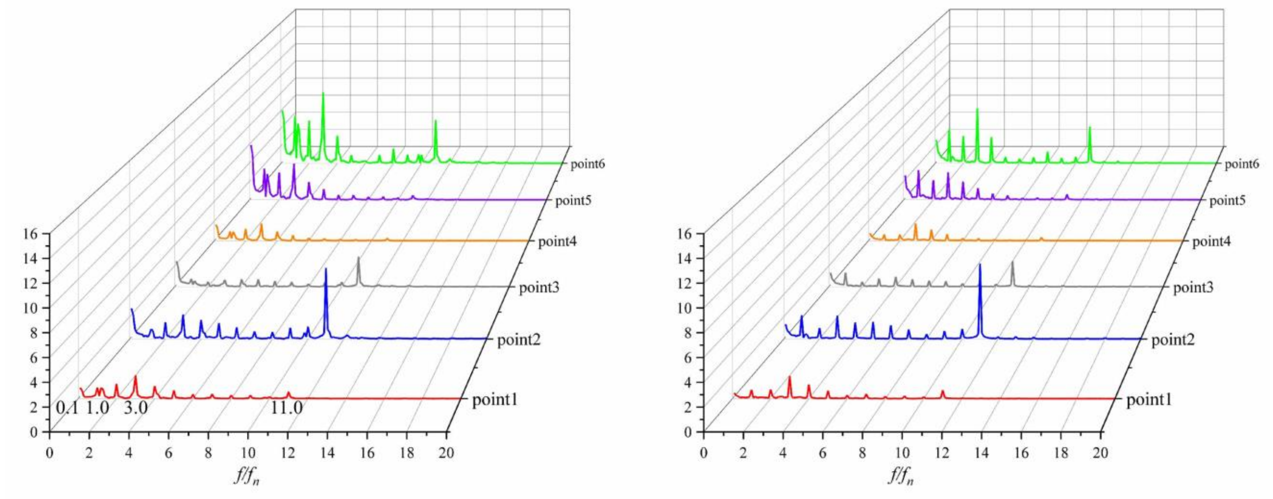

(a) FFT of velocity fluctuation at ITC=0.6mm

(b) FFT of velocity fluctuation at ITC=0.8mm

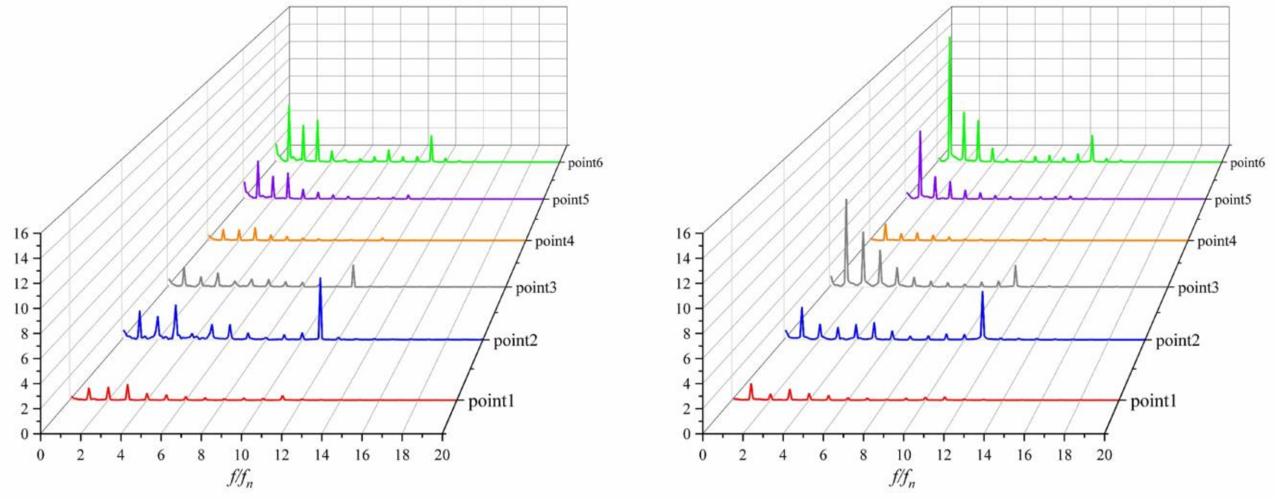

(c) FFT of velocity fluctuation at ITC=1mm

(d) FFT of velocity fluctuation at ITC=1.2mm

Fig. 22 FFT of pressure fluctuation at different inlet tip clearance

The total pressure ratio decreases as the ITC increases, while the polytropic efficiency first increases before decreasing.

Additionally, as the ITC rises, the operating range of the compressor expands, whereas its peak efficiency shifts to lower mass flows. The internal flow field analysis indicates a non-linear relationship between pressure, velocity, and load at the blade tip and the ITC, resulting in a non-linear change in aerodynamic performance relative to the ITC. There is periodicity in the spatial and temporal evolution of TLV.

Finally, the pressure and velocity fluctuation distribution at the monitoring points reveals that increasing the ITC reduces fluid flow resistance in the top region of the blade passage. This further confirms the physical mechanism behind the expanded operational range of the compressor. Pressure and velocity spectrum analysis indicates the impact of TLF is greater at the top of the impeller than it is at the bottom and middle. Moreover, the influence of TLF increases toward the bottom of the PS and SS and decreases near the middle and top of the PS as ITC rises.

The characteristics of pressure and velocity fluctuations, the TLV, and the FFT analysis provide valuable physical insights for understanding the steady and transient internal complex flow characteristics of a centrifugal compressor.

ACKNOWLEDGEMENTS

This work was supported by the National Natural Science Foundation of China (U22A20589), Natural Science Foundation Key Projects of Zhejiang Province (LZ22E060002), Zhejiang Province Science and Technology Innovation Team Project (2021R1009), Major Scientific and Technological Project of Zhejiang Province (2024C01176) Open Foundation of State Key Laboratory of High-end Compressor and System Technology, No.SKL-YSJ202301.

CONFLICT OF INTEREST

The authors declare there are no known conflicts of interest associated with this publication and there has been no significant financial support for this work that could have influenced its outcome. We confirm that the paper has been read and approved by all named authors and that there are no other persons who satisfied the criteria for authorship but are not listed.

AUTHORS CONTRIBUTION

Y. Zhang: Writing—Original Draft Preparation; **J. Chen:** Data Curation; **Y. Shu:** Data Curation, Review & Editing; **Y. Wei:** Review & Editing, Project Administration; **Z. Wang:** Modifications of Language; **H. Yang:** Modifications of Figures. All authors have read and agreed to the published version of the manuscript.

REFERENCES

Berdanier, R. A., & Key, N. L. (2015). Experimental investigation of factors influencing operating rotor tip clearance in multistage compressors. *International Journal of Rotating Machinery*,1–13. https://doi.org/10.1155/2015/146272

Chen, Y., Wang, Z., Yang, H., Zhang, W., & Wei, Y. (2022). Spatiotemporal characteristics and pressure fluctuations of internal flow in a high-speed centrifugal blower for vacuum cleaner at low flow-rate conditions. *Journal of Applied Fluid Mechanics*, *16*(2), 375-388. https://doi.org/ 10.47176/jafm.16.02.1245

Ekradi, K., & Madadi, A. (2020). Performance improvement of a transonic centrifugal compressor impeller with splitter blade by three-dimensional optimization. *Energy*, *201*. https://doi.org/10.1016/j.energy.2020.117582

Galindo, J., Tiseira, A., & Navarro, R. (2015). Influence of tip clearance on flow behavior and noise generation of centrifugal compressors in near-surge conditions. *International Journal of Heat and Fluid Flow*, *52*, 129–139. https://doi.org/10.1016/j.ijheatfluidflow.2014.12.004.

Hosseinimaab, S. M., & Tousi, A. M. (2022). Optimizing the performance of a single-shaft micro gas turbine engine by modifying its centrifugal compressor design. *Energy Conversion and Management*, *271*, 116245. https://doi.org/10.1016/j.enconman.2022.116245.

Jaatinen, A., Tiainen, J., & Turunen, T. (2016). Centrifugal compressor tip clearance and impeller flow. *Journal of Mechanical Science and Technology*, *30*, 5029-5040. https://doi.org/10.1007/s12206-016-1022-8

Ju, Y., Liu, Y., Jiang, W., & Zhang, C. (2021). Aerodynamic analysis and design optimization of a centrifugal compressor impeller considering realistic manufacturing uncertainties. *Aerospace Science and Technology*, *115*, 106787. https://doi.org/10.1016/j.ast.2021.106787.

Li, Y., Zhang, B., Chen, Y., Wang, Z., Yang, H., & Wei, Y. (2023). Temporal flow characteristics of three-dimensional centrifugal impeller suction system at vacuum conditions. *Journal of Applied Fluid Mechanics*, *16*(12), 2540-2555. https://doi.org/10.47176/jafm.16.12.1875

Liu, C., Tong, Z., & Ju, P. (2022). Effect of tip clearance on aerodynamic performance of supercritical carbon dioxide centrifugal compressor. *Turbine Technology*. *64*, 183-186+176. https://doi.org/10.1016/j.energy.2020.117582

Liu, F., Zhang, S. Y., & Shang, J. (2021). Influence of tip gap form on aerodynamic performance of cold compressor. *Cryogenics & Superconductivity*, *49*(8), 49-57. https://doi.org/10.16711/j.1001-7100.2021.08.010

Liu, Z., & Chen, L. (2012). Nature of tip clearance flow in subsonic unshroud impeller of centrifugal compressor. *Journal of Aerospace Power*, *27*(4), 937-945. https://doi.org/10.13224/j.cnki.jasp.2012.04.007

Ma, Y., Qian, B., & Feng, Z. G. (2021). Flow behaviors in a Kaplan turbine runner with different tip clearances. *Advances in Mechanical Engineering*, *13*(5), 1-15. https://doi.org/10.1177/16878140211015879

Mao, X., & Liu, B. (2017). Numerical investigation of tip clearance size effect on the performance and tip leakage flow in a dual-stage counter-rotating axial compressor. *Proceedings of the Institution of Mechanical Engineers, Part G: Journal of Aerospace Engineering*. *231*(3), 474-484. https://doi:10.1177/0954410016638878

Ostad, M., & Kamali, R. (2019). An investigation on the effect of blade tip clearance on the performance of a single-stage axial compressor. *Journal of Applied Fluid Mechanics*, *12*(3), 743-749. https://10.29252/jafm.12.03.29170

Schleer, M., Song, S. J., & Abhari, R. S. (2008). Clearance effects on the onset of instability in a centrifugal compressor. *Journal of Turbomachinery*, *130*, 13–23. https://doi.org/10.1115/1.2776956

Sohail, M. U., Hamdani, H. R., & Pervez, K. (2020). CFD analysis of tip clearance effects on the performance of transonic axial compressor. *Fluid Dynamics*, *55*(1), 133-144. https://doi.org/10.1134/S0015462820010127

Song, M. R., Xie, H. R., & Yang, B. (2020). Influence of tip clearance on flow characteristics of axial compressor. *Processes*, *8*(11), 1445-1464. https://doi:10.3390/pr8111445

Taghavi-Zenouz, R., & Eslami, S. (2012). Numerical simulation of unsteady tip clearance flow in an isolated axial compressor rotor blades row. *Proceedings of the Institution of Mechanical Engineers, Part C: Journal of Mechanical Engineering Science*, *226*(1), 82-93. https://doi.org/10.1177/0954406211412154

Tang, X., Gu, N., Wang, W., & Wang, Z. (2021). Aerodynamicrobustness optimization anddesign exploration of centrifugal compressorimpeller under uncertainties. *International Journal of Heat and*

MassTransfer, *80*. https://doi.org/10.1016/j.ijheatmasstransfer.121799.

Tsoutsanis, E., Meskin, N., & Benammar, M. (2015) . Transient gas turbine performance diagnostics through nonlinear adaptation of compressor and turbine maps. *Journal of Engineering for Gas Turbines and Power, 137*(9). https://doi.org/10.1115/1.4029710

Wang, S., Liu, Y. B., & He, X. (2020). Analysis of the influence of tip clearance on aerodynamic performance of transonic centrifugal compressor. *Turbine Technology, 62*(1), 4. https://CNKI:SUN:QLJV.0.2020-01-006

Xiang, J., Schluter, J., & Duan, F. (2019). Numerical study of the tip clearance flow in miniature gas turbine compressors. *Aerospace Science and Technology, 93*, 105352. https://doi.org/10.1016/j.ast.2019.105352.

Xu, Q. Y., Wu, J., & Wei, Y. K. (2022). Pressure and velocity fluctuations characteristics of the tip clearance flow in an axial compressor stage at the near-stall condition. *Aerospace Science and Technology, 129*. https://doi.org/10.1016/j.ast.2022.107796

Zamiri, A., Lee, B. J., & Chung, J. T. (2017). Numerical evaluation of transient flow characteristics in a transonic centrifugal compressor with vaned diffuser. *Aerospace Science and Technology, 70*, 244–256. https://doi.org/10.1016/j.ast.2017.08.003.

Zeng, Y.,Wang, H. B., & Sun, M. B. (2023). Review on SST turbulence Model improvements. *Acta Aeronautica ET Astronautica Sinica, 44*, 103-134. https://doi.org/10.7527/S1000-6893.2022.27411

Zhang, C., Dong, X., & Liu, X. (2019). Numerical simulation of tip leakage vortex trajrctory and stall prediction for centrifugal impeller. *Journal of Aerospace Power, 34*, 1586–1597. https://doi.org/10.13224/j.cnki.jasp.2019.07.020

Zhao, Y., Yan, C., Wang, X., Liu, H., & Zhang W. (2019). Uncertainty and sensitivity anal-ysis of SST turbulence model on hypersonic flow heat transfer. *Int. j. HeatMass Transfer 136* (JUN) 808-820. https://doi.org/10.1016/j.ijheatmasstransfer.2019.03.012.

Zheng, B., Shao, R., Zhang, S., Zhu, M, Qiang, X., & Teng, J. (2024). Optimization and experimental study ofstationary endwall of stator labyrinth cavity in low-speed research compressor. *Aerospace Science and Technology, 147*, 109036. https://doi.org/10.1016/j.ast.2024.109036

Zhu, W., Cai, L., & Wang, S. (2020) . Effect of tip clearance dimension on unsteadiness in a low-reaction aspirated transonic compressor rotor. *Proceedings of the Institution of Mechanical Engineers, Part G: Journal of Aerospace Engineering, 234*, 1181–1194. https://doi.org/10.1177/0954410019897467